Assessment of Climate Biases in OpenIFS Version 43R3 across Model Horizontal Resolutions and Time Steps

Abhishek Savita[1], Joakim Kjellsson[1,2], Robin Pilch Kedzierski[3,1], Mojib Latif[1,2], Tabea Rahm[1,2], Sebastian Wahl[1] and Wonsun Park[4,5]

[1]GEOMAR Helmholtz Centre for Ocean Research Kiel, Kiel, Germany
[2]Faculty of Mathematics and Natural Sciences, Christian Albrechts University of Kiel, Kiel, Germany
[3]Meteorological Institute, Universität Hamburg, Hamburg, Germany
[4]Center for Climate Physics, Institute for Basic Science (IBS), Busan, Republic of Korea
[5]Department of Climate System, Pusan National University, Busan, Republic of Korea

Correspondence to: Abhishek Savita (asavita@geomar.de)

Abstract.

We examine the impact of horizontal resolution and model time step on climate of the OpenIFS version 43R3 atmosphere general circulation model. A series of simulations for the period 1979-2019 are conducted with various horizontal resolutions (i.e., ~100, ~50, and ~25 km) while maintaining the same time step (i.e., 15 minutes) and using different time steps (i.e., 60, 30 and 15 minutes) at 100 km horizontal resolution. We find that the surface zonal wind bias reduces significantly over certain regions such as the Southern Ocean, the Northern Hemisphere mid-latitudes, and in tropical and subtropical regions at high horizontal resolution (i.e., ~25 km). Similar improvement is evident too when using a coarse resolution model (~100 km) with a smaller time step (i.e., 30 and 15 minutes). We also find improvements in Rossby wave amplitude and phase speed as well as weather regime patterns when a smaller time step or higher horizontal resolution is used. The improvement in the wind bias when using the shorter time step is mostly due to an increase in shallow and mid-level convection that enhances vertical mixing in the lower troposphere. The enhanced mixing allows frictional effects to influence a deeper layer and reduces wind and wind speed throughout the troposphere. However, precipitation biases generally increase with higher horizontal resolution or smaller time step, whereas the surface-air temperature bias exhibits a small improvement over North America and the Eastern Eurasian continent. We argue that the bias improvement in the highest horizontal resolution (i.e., ~25 km) configuration benefits from a combination of both the enhanced horizontal resolution and the shorter time step. In summary, we demonstrate that by reducing the time step in the coarse resolution (~100 km) OpenIFS model, one can alleviate some climate biases at a lower cost than by increasing the horizontal resolution.

1. Introduction

In the last few decades, Atmospheric-Ocean General Circulation Model (AOGCM) simulations from the Coupled Model Intercomparison Project (CMIP) have been widely used to study the internal climate variability and the climate response to external forcing such as increasing atmospheric greenhouse gas concentrations causing global warming. These simulations, however, suffer from long-standing biases (**Bayr et al., 2018; Flato et al., 2014; Gates et al., 1999; Kim et al., 2014; Zhou et al., 2020**), which lead to significant uncertainties in short-term and long-term climate projections and potential ecosystem impacts (**Athanasiadis et al., 2022; Couldrey et al., 2021; Meehl and Teng, 2014; Meng et al., 2022**). These biases can arise from a variety of sources, including inaccurate representation of physical processes, poor initialization of model conditions, or inadequate representation of the Earth's topography and land cover.

Simulations using Atmospheric General Circulation Models (AGCMs) from the Atmosphere Model Intercomparison Project (AMIP), a part of CMIP, are used to study the internal variability of the atmosphere. The AGCMs are less complex than the AOGCMs as the former are constrained by observed Sea Surface Temperature (SST) and Sea Ice Concentration (SIC). Despite being constrained by the observations, the AGCMs also exhibit biases (**e.g., Gates et al., 1999**), and some of these biases have persisted for over several phases of AMIP (**He and Zhou, 2014**). The biases in AGCMs are largely due to the fact that many unresolved processes, such as atmospheric convection, precipitation, clouds, cloud-microphysical and aerosol processes, boundary layer processes, and interactions between the land surface and hydrologic processes, have to be included in a parameterized form in the coarse resolution model (**Ma et al., 2022**). The treatment of unresolved gravity waves and the relatively large model time step also contribute to the biases in AGCMs (**Flato et al., 2014; Gates et al., 1999**).

Recently, **Liu et al. (2022)** analyzed AOGCM simulations and reported that increasing the horizontal resolution of the ocean component one can reduce SST and precipitation biases in the equatorial Pacific, whereas increasing the horizontal resolution of the atmospheric component did not have the same effect. However, other studies found that a high-horizontal resolution atmosphere model better simulates the main features of tropical precipitation, tropical atmospheric circulation, and extra-tropical cyclones while increasing from 125 km to 40 km horizontal resolution with relatively small improvements for further enhanced horizontal resolution (**Branković and Gregory, 2001; Jung et al., 2012; Williamson et al., 1995**). Similarly, **Roberts et al. (2018)** found that there was not much improvement in the Integrated Forecasting System (IFS) from the European Centre for Medium-Range Weather Forecasting (ECMWF) when increasing horizontal resolution from 50 to 25 km.

Jung et al. (2012) and **Roberts et al. (2018)** demonstrated a time step sensitivity in the coarse and high horizontal resolution model simulations using the IFS model. **Jung et al. (2012)** found that the precipitation and wind biases were reduced at the

coarse horizontal resolution when shortening the model time step from 60 to 15 minutes. **Roberts et al. (2018)** did not find such a significant improvement when reducing the model time step from 20 to 15 minutes in their high-resolution (~25 km) configuration. However, both studies did not investigate the model's sensitivity to changes in the model time step in detail. While the semi-implicit semi-Lagrangian scheme, as used in OpenIFS, is unconditionally stable and the time step can be chosen to be very long, a shorter time step generally leads to a decrease in truncation error in the finite differences and thus a more accurate representation of the model dynamics. The physics parameterisations, which are computed independently of each other in OpenIFS, also benefit from a shorter time step as it will allow the various parameterisations to be coupled at a higher frequency **(Beljaars et al., 2018)**. However, model parameters for e.g., convection or diffusion may be tuned for a specific time step and shortening the time step can therefore, in some cases, increase model error. Hence, a shorter model time step is expected to reduce biases in model dynamics, e.g., winds, while the results for parameterised processes, e.g., precipitation, may be mixed.

In the research community, there is no standard definition for coarse horizontal resolution, as one study considered 200 km as a coarse resolution (~2°) configuration (**Branković and Gregory,** 2001), whereas another study considered 50 km (0.5°) as a coarse resolution (**Roberts et al., 2018**). Likewise, there is no unique rule for setting the model time step dependent on model resolution. Groups using either the IFS or OpenIFS model at horizontal resolutions of ~100 km have used a relatively long time step of 1 hour (**Hazeleger et al., 2012; Kjellsson et al., 2020; Streffing et al., 2022**) or 45 minutes (**Döscher et al., 2022**), while other groups using the ARPEGE-Climat with a similar dynamical core use 15 minutes (**Voldoire et al., 2019**). The model's horizontal resolution and time steps are rather chosen on what can be afforded computationally, and their relative contributions to biases in the model's climate are not well documented.

In this study, we systematically investigate the sensitivity of the OpenIFS model version 43r3v2 to the model time step and horizontal resolution. We mostly focus on the surface zonal winds since they play a crucial role for the ocean circulation in the AOGCMs. We also study the representation of the synoptic-scale variability such as Rossby waves and weather regimes. The paper is structured as follows: section 2 describes the model, experimental design, data and methodology; section 3 describes the results and section 4 summarizes the conclusions of this work.

2. Model, Experimental design, Data and Methodology

We conducted a series of experiments with the OpenIFS model. The OpenIFS model is derived from the Integrated Forecasting System at the European Centre for Medium-range Weather Forecasting (ECMWF-IFS) cycle 43 release 3 (43r3). The dynamical core is the same as ECMWF-IFS that uses a two-time-level semi-implicit time stepping with semi-Lagrangian advection **(Temperton et al., 2001)** on a reduced Gaussian grid with a hybrid-sigma vertical coordinate **(Simmons and Burridge, 1981)**. Likewise, the OpenIFS uses the same model physics as the ECMWF-IFS **(cf. Forbes and Tompkins, 2011;**

104 **Hogan and Bozzo, 2018; Tiedtke, 1993)** but does not include the tangent-linear code or 4D-VAR capabilities. Our version,

105 OpenIFS, is similar to cy43r1 used in **Roberts et al., (2018)**, with the main difference being the new radiation scheme, ecRad

106 (**Hogan and Bozzo, 2018**), introduced in cy43r3.

107

108 Our study is partly motivated by evaluating the suitability of various OpenIFS configurations for coupled climate simulations

109 with FOCI-OpenIFS (**Kjellsson et al.**, 2020) with an atmosphere horizontal resolution higher than that of ECHAM6 Tq63/N48

110 (~200km) in FOCI (**Matthes et al., 2020**). Our choices thus fall on three different horizontal resolutions: a low-resolution

111 (T_{co}95, ~100 km), a medium-resolution (T_{co}199, ~50 km), and a high resolution (T_{co}399, ~25 km). The T_{co}95 grid is the lowest

112 acceptable resolution since the supported lower-resolution grids, e.g., Tl95/N48 and Tq42/F32, are either similar to Tq63 in

113 ECHAM6 or coarser. The T_{co}399 grid was chosen as an upper limit of what is computationally feasible for AMIP integrations

114 and century-long coupled integrations given our computer resources. All the configurations share the same vertical L91 grid.

115 We did not modify any other model parameters when changing the model horizontal resolutions or model time steps, but we

116 note that some parameters such as launch momentum flux for non-orographic gravity waves scales with resolution in the

117 model. We performed 5 experiments in total (**Table 1**). For simplicity, we now refer now OpenIFS as OIFS in the rest of the

118 sections.

119

120 The lower boundary conditions, i.e., SST and SIC, are taken the from Atmospheric Model Intercomparison Project (AMIP)

121 version 1.1.6 (**Eyring et al., 2016; Taylor et al., 2012**), which are available as monthly means on a 1°x1° horizontal grid. The

122 external forcing is identical to that used in the CMIP6 AMIP simulations except for the aerosol and ozone concentrations,

123 which are taken from monthly mean climatology. SST and SIC are interpolated from monthly to daily frequency and from

124 1°x1° horizontal resolution to the OIFS horizontal grid using bilinear interpolation. All the simulations are run for the period

125 1979–2019. We extend the simulations beyond the AMIP protocol for 1979-2014 up to 2019 by using SST and SIC from the

126 ERA5 reanalysis and the Shared Socioeconomic Pathways 5 (SSP5-8.5) emission scenario. Ozone concentrations are taken

127 from monthly photochemical equilibrium state and aerosol concentrations from monthly CAMS climatology of 11 species.

128

129 Amplitude and phase speed of Rossby wave were computed by performing a Fourier decomposition analysis on 300 hPa daily

130 meridional winds. First, we interpolated both ERA5 and OIFS simulation datasets onto a 2.5° x 2.5° grid using bilinear

131 interpolation. We then applied the Fourier decomposition analysis to determine amplitude and position for each Rossby wave

132 number at each latitude as a function of time. Phase speed is computed as the difference in the daily position of each wave,

133 and stored at the midpoints in the time dimension. For consistency, wave amplitudes are interpolated to the midpoints in time

134 as well. Lastly, seasonal averages are computed from the daily data for the boreal and austral winter seasons over the time

135 period 1979–2019. In the case of phase speed, it is weighed by the corresponding daily (midpoint) amplitude squared when

136 computing the seasonal averages in order to account for the impact of higher-amplitude events. The results are presented in

137 wavenumber-latitude diagrams similar to previous studies (**e.g., Pilch Kedzierski et al., 2020; Wolf and Wirth, 2017**). Our

---

144 wavenumber-latitude analysis is not directly comparable to both studies mentioned above, because we did not apply any high-

145 pass filtering in time before the Fourier decomposition. While the previous literature had similar diagrams with varying

146 measures of wave amplitude, our detailed analysis of phase speed in such a manner is novel in literature to our knowledge and

147 a strong addition as a model performance diagnostic.

148

149 The Weather Regime Patterns (WRPs) were calculated using daily 500-hPa geopotential height (z500) anomalies over the

150 Euro-Atlantic region (30°–90 °N, 80 °W–40 °E) for the boreal winter season during the period 1979-2019. The daily z500

151 daily anomalies were computed by subtracting the daily climatology smoothed by a 20-day running mean from the raw z500

152 data. We calculated the first four Empirical Orthogonal Functions (EOFs) from the ERA5 dataset. In the next step, the OIFS-

153 simulated z500 anomalies were projected on the ERA5 EOFs to obtain Pseudo-Principal Components (Pseudo-PCs). We then

154 applied a K-means clustering algorithm to the individual model pseudo-PCs and observation PCs using four clusters. We chose

155 four clusters because these give the most of the significant clustering. Spatial WRPs are obtained by compositing over all daily

156 z500 anomalies for each regime. More information about the methodology can be found in **Fabiano et al. (2020),** section 3.1.

157 In order to evaluate the WRPs simulated by the OIFS across configurations more quantitatively, we have additionally estimated

158 the Pearson's Pattern Correlation Coefficient (PCC) between the WRPs identified in the model and ERA5.

159

160 We compare the climate of OIFS to observational and reanalysis datasets. Precipitation is validated against the Global

161 Precipitation Climatology Project **(GPCP; Huffman et al., 1997)**, and the surface air temperature (SAT) against the

162 CRUTEM4 **(Harris et al., 2014; Osborn and Jones, 2014).** We have used the ERA5 reanalysis **(Hersbach et al., 2020)** to

163 evaluate 10-meter surface wind as well as the zonal wind at 300 hPa for the Rossby wave analysis. We use z500 from ERA5

164 to validate the OIFS-simulated weather regimes. We also compare our results with the MERRA2 reanalysis **(Gelaro et al.,**

165 **2017)** and find similar results. Therefore, the comparison with MERRA2 is not shown. The bootstrapping (in total 2000

166 iterations) method is used to compute the 95% confidence interval for the RMSE and the WRPs correlation.

167 **3. Results**

168 **3.1.1 Global and regional surface bias and deriving processes**

169 The annual mean 10m zonal wind (surface wind hereafter) bias during the period 1979–2019 for the different OIFS

170 configurations is shown in **Fig. 1**. We find that the OIFS-LRA-1h configuration has a large surface wind bias over most of the

171 world ocean, with positive biases in the mid-latitudes (the Southern Ocean, North Atlantic and North Pacific) and negative

172 surface wind biases over the tropical oceans (Tropical Pacific, Tropical Indian and Atlantic Ocean) **(Fig. 1b)**. Thus, the OIFS-

173 LRA-1h configuration simulates too strong surface westerly winds (and wind speed) over the mid-latitude oceans, which, if

174 coupled to an ocean model, may cause biases in upper-ocean mixing and oceanic uptake of heat and carbon.

175

176 The surface wind bias in the OIFS-HRA-15m configuration is reduced significantly (**Fig. 1f**) over most of the world ocean
177 compared to the OIFS-LRA-1h configuration (**Fig. 1b**), indicating that increasing the horizontal resolution from 100 km to 25
178 km and shortening the time step from 1h to 15-min improves the representation of the surface winds. The surface wind bias
179 also significantly reduces everywhere in the OIFS-MRA-15m configuration **(Fig. 1e)** compared to the OIFS-LRA-1h
180 configuration **(Fig. 1b)**. The surface wind bias in OIFS-MRA-15m is larger than that in the OIFS-HRA-15m configuration but
181 smaller than that in the OIFS-LRA-1h configuration. Similar conclusions are obtained by performing Root Mean Square Error
182 (RMSE) analysis, which shows that the OIFS-HRA-15m configuration has the lowest annual and global mean RMSE of
183 surface wind while the OIFS-LRA-1h configuration has the highest RMSE (**Fig. 2a, black line**). Though we have found a
184 significant improvement in the wind bias in the OIFA-HRA-15m configuration, it is not clear yet whether the improvement is
185 due to the increased horizontal resolution or the shorter time step.
186
187 Surface wind bias is also reduced in both the OIFS-LRA-30m (**Fig. 1c**) and OIFS-LRA-15m (**Fig. 1d**) configurations compared
188 to the OIFS-LRA-1h configuration (**Fig. 1b**), and the bias improvement is mostly observed at the same places as in the OIFS-
189 HRA-15m configuration (**Fig. 1f**). The surface-wind bias improvement is similar in the OIFS-LRA-30m and OIFS-LRA-15
190 configurations, except over the North Pacific and Southern Ocean where the OIFS-LRA-15m configuration has a smaller wind
191 bias than the OIFS-LRA-30m configuration. However, we have not seen a large difference between the OIFS-LRA-30m and
192 OIFS-LRA-15 configurations in the global average RMSE analysis (**Fig. 2a**).
193
194 The surface-wind bias improvement in the OIFS-HRA-15m and OIFS-LRA-15m configurations not only exists in the annual
195 average but also in boreal winter (DJF) and summer (JJA) (**Fig. 2a blue and red lines**, respectively). Our results are consistent
196 with **Jung et al. (2012)**, as they found a reduction in wind bias in the tropical Pacific region when they shortened the time step
197 in their coarse resolution configuration. However, this study and the **Jung et al. (2012)** study are not consistent with that of
198 **Robert et al. (2020)** who did not find much time-step sensitivity. We speculate that in **Robert et al. (2020),** the reduction
199 from 20 to 15 minutes in their high horizontal resolution (25 km) may be too small. Alternatively, the 20-minute time step
200 could be the optimal time step for the 25 km configuration.
201
202 The surface wind bias in the OIFS-HRA-15m and OIFS-LRA-15m configurations looks similar in pattern, but they differ in
203 magnitude. The OIFS-HRA-15m configuration has a smaller bias in the North Pacific, Peru upwelling and Agulhas Bank
204 regions compared to the OIFS-LRA-15m configuration. We hypothesize that the reduction in surface-wind bias in the OIFS-
205 HRA-15m configuration (**Fig. 1f**) compared to the OIFS-LRA-1h configuration (**Fig. 1b**) is a combination of the enhanced
206 horizontal resolution and shorter time step. The improvement in the OIFS-HRA-15m configuration (**Fig. 1f**) compared to the
207 OIFS-LRA-15m configuration (**Fig. 1d**) is due to only the enhanced horizontal resolution as both configurations use the same
208 time step.
209

211 The zonal-wind bias improvement in the OIFS-LRA-15m is further explored using the online zonal wind tendencies from
212 OIFS which are split into dynamics and physics that includes turbulent diffusion, gravity-wave drag and convection:

214 $$du/dt = du/dt_{Dyn} + du/dt_{Turb} + du/dt_{Gwd} + du/dt_{Conv} \qquad (1)$$

216 where du/dt_{Dyn} is the sum of the tendencies from advection, pressure gradient and Coriolis force, du/dt_{Turb} includes tendencies
217 from surface processes, vertical diffusion and orography drag, du/dt_{Gwd} includes gravity-wave drag and non-orographic drag,
218 and du/dt_{conv} is the tendency from convection. The individual tendencies on the right-hand side of equation (1) are referred to
219 as Dyn, Turb, Gwd and Conv, respectively. They were stored for each model level in the OIFS-LRA-1h and OIFS-LRA-15m
220 configurations. The lowest model level is at 10m height (assuming surface pressure of 1013hPa), so the 10m wind will behave
221 very similarly to the wind at level k=91.

223 The averaged zonal wind and zonal wind tendencies over the Southern Ocean (40º S – 60º S and all longitude) in the OIFS-
224 LRA-1h and OIFS-LRA-15m configurations are shown in **Fig. 3a & b,** respectively. The zonal wind tendency (i.e., du/dt) in
225 both OIFS-LRA-15m and OIFS-LRA-1h configurations is very small (~-2 to 0.04 m/s^{-1}) compared to the other processes (**Fig.**
226 **3b, black lines**). Conv provides westward acceleration between the 700 and 900 hPa pressure levels and eastward acceleration
227 below, indicating a downward transport of westward momentum. Dyn acts to accelerate the flow eastward from 700 hPa and
228 below, likely via momentum advection, pressure-gradient and Coriolis forces, while Turb has the opposite effect, likely via
229 surface friction and vertical mixing processes. In the OIFS-LRA-15m configuration, we find a similar balance as in the OIFS-
230 LRA-1h, but the westward acceleration above and eastward acceleration below is enhanced by Conv, likely by increased
231 downward momentum transport, in agreement with the increased shallow and mid-level convection (**Fig. 3d**). The vertical
232 momentum mixing by shallow and mid-level convection reduces the vertical wind shear, making the westerly winds more
233 barotropic. As a result, the westerly winds weaken throughout the troposphere and even in the stratosphere (**Fig. 3a**). We note
234 similar changes in the Northern Hemisphere mid-latitudes, suggesting similar mechanisms are acting. Gwd has a negligible
235 role for the winds in the lower stratosphere and troposphere, and the Gwd term does not appear sensitive to model time step
236 (**Fig. 3b, orange lines**).

238 **Fig. 3c** shows the zonal average of the zonal wind tendencies at the lowest level of the model, as a function of the latitude. In
239 the OIFS-LRA-1h configuration, Conv and Dyn accelerate the surface westerly wind in the mid-latitudes (~40º N to ~60º N)
240 in both hemispheres, and these westerly winds are partly balanced by Turb (**Fig. 3c, solid lines**). Dyn has a larger contribution
241 to accelerating the surface westerly winds than Conv (**Fig. 3c, solid lines**). However, the Conv contribution is enhanced in the
242 OIFS-LRA-15m configuration, while the Dyn contribution reduces (**Fig. 3c, dashed lines**). We also find that the contribution
243 to slowing the westerly wind is reduced by Turb in the OIFS-LRA-15m configuration (**Fig. 3c, dashed lines**).

244

245 It is also noteworthy that the individual wind tendencies contribute significantly more in the Southern Hemisphere than in the

246 Northern Hemisphere (**Fig. 3c**). In the low latitudes, both Dyn and Conv contribute to accelerating the easterly winds, which

247 is partly balanced by Turb in the OIFS-LRA-1h configuration (**Fig. 3c, solid lines**). There are no discernible changes in Conv,

248 Dyn or Turb from OIFS-LRA-1h to OIFS-LRA-15m, indicating that the tropical surface winds are relatively insensitive to

249 model time step (**Fig. 3c, dashed lines**).

250

251 In addition to surface wind, we also investigated the sensitivity of model time step and horizontal resolution for SAT and

252 precipitation. The RMSEs for SAT and precipitation are shown in Figure 2b and 2c, respectively. We find that the OIFS-HRA-

253 15m has the lowest SAT RMSE of all model experiments in both annual and seasonal means, although the RMSE difference

254 across the configurations is not significant (**Fig. 2b**). The reduced SAT RMSE in OIFS-HRA-15m configuration is primarily

255 due to the lowered SAT bias over North America and the eastern part of Russia. Compared to the OIFS-LRA-1h, the SAT

256 RMSE decreases with increased horizontal resolution (OIFS-HRA-15m and OIFS-MRA-15m), and there is no notable

257 improvement when shortened the time step (OIFS-LRA-30m and OIFS-LRA-15m) (Fig 2b).

258

259 We have computed the SAT and precipitation biases with a 3-point smoothing, i.e., approximately 3x3 degree spatial

260 smoothing, which eliminates the wiggles near steep topography arising from the Gibbs' phenomenon in the model spectral

261 fields. We find that smoothing the fields does not change the main result that precipitation biases increase with shorter time

262 step in Tco95 and then decreases somewhat with higher horizontal resolution. Hence, the wiggles are not the main source of

263 precipitation biases and their presence does not impact the findings in this study.

264

265 The OIFS-LRA-1h experiment exhibits the lowest precipitation RMSE of all experiments, with RMSE increasing with shorter

266 time step (OIFS-LRA-15m) and increased horizontal resolution (OIFS-HRA-15m) for both the annual and boreal winter means

267 (**Fig. 2c, black and blue lines**). The patterns of regional precipitation biases are similar across the configurations in the mid-

268 and high-latitudes, whereas the precipitation biases increase in the tropics at the high horizontal resolution or in the smaller

269 time step configuration (not shown). The results suggest that some of the cloud and/or convection parameters may be dependent

270 on resolution or time step and need retuning for each configuration.

271 **3.1.2 Wind and temperature bias in upper-atmosphere**

272 We examined the zonal mean u wind bias at different model levels, and it is shown in Figures 4. We find that zonal mean u

273 wind bias over the tropical region (40ºS and 40ºN) is positive and independent of model horizontal resolution and model time

274 step (Fig. 4b-f). The OIFS-HRA-15m configuration has a relatively large negative bias in the Northern Hemisphere compared

275 to the other configurations. The OIFS-LRA-15m and OIFS-HRA-15m zonal mean u wind bias is similar to that in Robert et

276 al. (2018). However, the zonal mean u wind bias in the Southern Hemisphere is not consistent across horizontal resolution or

277 model time step. The zonal mean u wind bias in midlatitudes (i.e., 70ºS to 50ºS) is positive and large in the OIFS-LRA-1h

Deleted: T

Deleted: also

Deleted: figure not shown

281 configuration and reduces throughout the pressure levels by shortening the model time step in the coarse resolution OpenIFS

282 configuration (i.e., OIFS-LRA-30m and OIFS-LRA-15m). Whereas, the negative zonal wind bias south 70ºS in the coarse

283 resolution configuration is consistent across the different time steps (Fig. 3b-d). It is also interesting to note that both OIFS-

284 MRA-15m and OIFS-HRA-15m configurations exhibit a negative bias over the Southern Ocean (SO) at most of the pressure

285 levels, which is not seen in the standard OIFS-LRA-1h, nor in the OIFS-LRA-30m or OIFS-LRA-15m configurations. Overall,

286 we conclude that by reducing the model time step in the coarse resolution configuration, we improve winds not only at the

287 surface but also at higher model levels mostly over the SO. A similar conclusion does not hold for the OIFS-MRA-15m and

288 OIFS-HRA-15m configurations, as both suffer from large negative bias over the SO.

289

290 We also examined the zonal mean temperature bias at different pressure levels. We find a cold bias (1.5 to 6 °C) in the

291 troposphere and lower stratosphere, and a warm bias (1.5 to 6 °C) above the stratosphere across the configurations (Figure not

292 shown). This indicates that OpenIFS simulations (independent of model time step and horizontal resolution) are colder than

293 observations in the lower stratosphere and warmer above. The cold bias in the lower stratosphere is larger in the high resolution

294 (i.e., OIFS-HRA-15m), and the warm bias above the stratosphere is smaller compared to the other configurations. Robert et

295 al. (2018) noticed a similar zonal mean temperature bias and speculated that the zonal mean temperature bias is linked with

296 the sensitivity of spurious mixing due to convection and diffusion.

297 **3.2 Rossby wave analysis**

298 **Fig. 5** shows the Rossby wave amplitude (gray and black contours) for ERA5 and the individual OIFS simulations for the

299 boreal winter (**Fig. 5A, DJF, Northern Hemisphere; NH)**) and austral winter (**Fig. 5B, JJA, Southern Hemisphere; SH**).

300 The color in **Fig. 5** denotes the wave amplitude bias relative to ERA5 (model – ERA5). We focus only on those wave numbers

301 and latitudes that have the highest wave amplitude, because these waves explain most of the variability. The region where the

302 wave amplitude is larger than 5 ms^{-1} is termed "core region", which mostly covers the area that is occupied by the thick black

303 contours in **Fig. 5**. In DJF (NH), at north of 70º N, the Rossby wave numbers k=1 and k=2 have the largest amplitude in ERA5

304 whereas at the mid-latitudes (30º N to 60º N), the wave numbers between about k=3 and k=9 have large amplitude with the

305 largest amplitude amounting to 8 ms^{-1} at about 40º N for the wave number k=6 (**Fig. 5Aa**). During JJA (SH), the wave

306 amplitude is located in a similar core region (**Fig. 5Ba**) as that in DJF (NH). The amplitude is largest south of 70º S for the

307 wave numbers k=1 and k=2 whereas at the mid-latitudes (45º S to 65º S), the wave numbers between about k=3 to 5 have large

308 amplitude with the largest amplitude amounting to 9 ms^{-1} is found at 57.5º S for the wave number k=4 (**Fig. 5Ba**).

309

310 In DJF (NH) the OIFS-LRA-1h configuration exhibits a positive bias of ~1 ms^{-1} in Rossby wave amplitude (i.e., the waves

311 amplitude bias in OIFS-LRA-1h is larger than the ERA-5) in the core region, in particular for wave numbers k=3-8 at latitudes

312 between 25º N to 55º N and a negative bias at latitudes between 60º N to 80º N for waver number 2 (**Fig. 5Af**). The wave

333 amplitude biases around the core region in OIFS-LRA-1h in the midlatitudes (20º N to 40º N) are small (~0.2) for the higher

334 wave numbers and get better with a shorter time step configuration (OIFS-LRA-15m).

335

336 The Rossby wave amplitude biases in the OIFS-HRA-15m configuration are strongly reduced compared to the OIFS-LRA-1h

337 configuration over the core region (**Fig. 5Ab and 5Af**). The Rossby wave amplitude bias reduction in the OIFS-MRA-15m

338 configuration is mostly similar to that in the OIFS-HRA-15m configuration except for the wave number k=7 at 45º N, where

339 the wave amplitude bias is larger in the OIFS-HRA-15m configuration (**Fig. 5Ab and 5Ac**). The OIFS-HRA-15 m and OIFS-

340 MRA-15m configurations also exhibit a positive bias for wave number 2 at high-latitudes 60º N to 80º N. The OIFS-MRA-

341 15m configuration also show a negative bias for the wave number 3 at latitudes between 60º N to 65º N in the core region,

342 which is not present in the other configurations. The OIFS-HRA-15m and OIFS-MRA-15m configurations show similar bias

343 around the core region as in the OIFS-LRA-1h configuration, i.e., high resolution and OIFS-LRA-1h configurations

344 overestimate wave amplitudes for the higher wave numbers. The Rossby wave amplitude biases are progressively reduced

345 from the OIFS-LRA-1h configuration to the OIFS-LRA-30m and OIFS-LRA-15m configurations (**Fig. 5Ad-Af**), indicating a

346 sensitivity of model bias to the time step. The wave amplitude bias for wave number k=7 at 45º N exists in all the

347 configurations, and it is smaller in the OIFS-LRA-15m and OIFS-MRA-15m configuration than in the other configurations.

348 Overall, both OIFS-LRA-15m and OIFS-HRA-15m configurations are able to reproduce the observed Rossby-wave

349 amplitudes in DJF (NH) better than OIFS-LRA-1h.

350

351 In JJA (SH), the Rossby wave amplitude bias in the core region is smaller than in DJF (NH) for all the configurations (**Fig.**

352 **5A and 5B**). OIFS-LRA-1h exhibits a positive bias of ~0.5 ms^{-1} in JJA (SH) for the wave number k=2 at latitude between ~50º

353 S and ~62.5º S and for wave numbers k=4 to 5 between 30º S and 40º S (**Fig. 5Bf**). The OIFS-LRA-30m configuration shows

354 a positive bias for the wave number k=2 to 5 at latitudes between 40º S and 70º S, which is larger than other configurations.

355 The OIFS-HRA-15m and OIFS-MRA-15m configurations exhibits a positive bias ~0.5 ms^{-1} around the core region and

356 latitude 50º S to 70ºS, which does not exist in the other coarse resolution configurations (**Fig. 5Bb-Bf**). The Rossby wave

357 amplitude biases around the core region at the midlatitudes in the high-resolution simulations are consistent and large in the

358 SH than the NH (Fig. 5Ab-c and 5Bb-c).

359

360 We also analyze the phase speed of Rossby waves for ERA5 and across the OIFS' configurations for DJF (NH) and JJA (SH)

361 seasons (**Fig. 6**). In the ERA5 dataset (**Fig. 6Aa**), the Rossby wave phase speed is positive (i.e., eastward moving, solid contour)

362 for wave numbers greater than 2 (i.e., k>2) at most latitudes. The wave numbers k=1 to 2 have a positive wave phase speed

363 from the equator to 55º N and a negative wave phase speed (i.e., westward moving, dashed contours) between 60º N and 80º

364 N in DJF (NH) (**Fig. 6Aa**). The maximum phase speed is found at wave number k=8 at 40º N, while the minimum is found at

365 wave number k=1 at 60º N (**Fig. 6Aa**). In JJA (SH) (**Fig. 6Ba**), the wave phase speeds are mostly positive and large for all the

392   wave numbers and at each latitude, with the maximum phase speed is observed for the wave numbers between k=6 and k=8

393   and latitudes between 40º S and 60º S, and these waves are moving faster than that in DJF (NH).

394

395   The OIFS-LRA-1h configuration suffers from positive phase speed bias for wave numbers k=4 to 8 at latitudes between 42.5º

396   N and 60º N, i.e., waves move faster eastward than in ERA5, and the bias is larger than 1 ms^{-1} for wave

397   number k = 6 to 8 at 40º N and 60º N is of particular concern as it is near the maximum wave amplitudes in DJF (**Fig. 6Af**).

398   In general, phase speed biases in the OIFS-LRA-1h configuration are strongly reduced as either horizontal resolution is

399   increased or time step is shortened (**Fig. 6Ab-5Af**). In JJA (SH), the OIFS-LRA-1h configuration exhibits a very large (between

400   ~1.5-2 ms^{-1}) Rossby wave phase speed bias for most of the wave numbers, which is largest for the wave numbers k=2 to 8

401   between 15º S to 55º S (**Fig. 6Bf**). Large biases can be found between 15º S and 25º S (~1.5 ms^{-1}) for most of the wave

402   numbers, but the wave activity is low there (**Fig. 6Bf**). The large phase speed biases are strongly reduced in the OIFS-LRA-

403   30m and OIFS-LRA-15m configurations (**Fig. 6Bd-Bf**), indicating a strong sensitivity to the reduced biases in mean winds

404   and wind speeds (**Fig. 1**). Overall, the Rossby wave speed bias in the OIFS-HRA-15m configuration is smaller than in the

405   OIFS-LRA-1h configuration (**Fig. 6Bb and 6Bf**). However, we note that both the OIFS-MRA-15m and OIFS-HRA-15m

406   configurations exhibit negative biases south of 55º S for wave numbers k= 1 to 5, that is, the eastward moving waves are

407   slower than in the ERA5 (**Fig. 6Bb**).

408

409   The wave phase speed analysis reveals a clear improvement in the representation of the Rossby waves in the boreal winter

410   (i.e., NH) when increasing the horizontal resolution and shortening the model time step compared to OIFS-LRA-1h

411   configuration. In austral winter, however, the representation of Rossby wave amplitudes and phase speeds are the most realistic

412   in OIFS-LRA-15m configuration, with longer time steps introducing too fast phase speeds and higher horizontal resolution

413   introducing too slow phase speeds at wave number less than 6 (i.e., k<6).

414   **3.3 Weather regimes pattern**

415   We derive the four weather regimes patterns (WRPs) over NH in the Euro-Atlantic region from ERA5. The patterns resemble

416   the positive and negative phases of the North Atlantic Oscillation (NAO+ and NAO–, respectively), Scandinavian blocking

417   (Sc. Blocking), and the North Atlantic ridge (Atl. Ridge) pattern (**Fig. 7, bottom row**). These WRPs are consistent with the

418   previous findings (**Dawson et al., 2012; Fabiano et al., 2020; Fabiano et al., 2021**).

419

420   The OIFS-HRA-15m configuration produces WRPs that are more visually similar to those in ERA-5 than does OIFS-LRA-1h

421   (Fig. 6), a result confirmed by the higher pattern correlation coefficient (PCC) between OIFS-HRA-15m and ERA5 compared

422   to the OIFS-LRA-1h and ERA-5 (**Fig. 7 and 8**). The PCCs for NAO+, NAO- and Sc. Blocking all exceed 0.8 in OIFS-HRA-

423   1h while OIFS-LRA-1h does not achieve PCC above 0.8 for any WRP (**Fig. 7**).

443

444   The OIFS-MRA-15m configuration shows smaller PCCs than both the OIFS-HRA-15m and OIFS-LRA-1h configurations
445   (**Fig. 8**), i.e., the improvement from OIFS-LRA-1h to OIFS-HRA-15m does not have a linear relationship with model
446   horizontal resolution or time step. Compared to other configurations and ERA5, OIFS-MRA-15m the z500 anomaly in the
447   NAO+ pattern is too elongated in the southwest-northeast direction, and an unrealistic negative z500 anomaly over the North
448   Atlantic appears in the Sc. Blocking regime (**Fig 7**). Furthermore, OIFS-MRA-15m shows an Atl. Ridge pattern with neither
449   the right structure nor amplitude.

450

451   There is an improvement in the representation of the NAO- regime in the OIFS-LRA-30m configuration over the OIFS-LRA-
452   1h configuration (**Fig. 7**) while the Sc. Blocking regime becomes worse due to the ridge shifting westward. These changes are
453   also reflected in the PCCs (**Fig 8**). Similarly, the OIFS-LRA-15m better represents NAO- and Atl. Ridge than OIFS-LRA-1h
454   while NAO+ and Sc. Blocking worsened. The westward shift of the Sc. Blocking is similar in OIFS-LRA-15m and OIFS-
455   LRA-30m, and the worse NAO+ is related to a northward shift of both the positive and negative z500 anomalies. We note that
456   all experiments use the same SST and sea-ice conditions and that OIFS-LRA-1h, 30m and 15m share the same horizontal
457   resolution, i.e., the changes from OIFS-LRA-1h to OIFS-LRA-15m are not due to SST biases or representation of orography.
458   There does not seem to be a clear improvement as time step is shortened, despite the reduction in mean state biases and Rossby-
459   wave amplitudes and phase speeds.

460

461   The PCC is greater than 0.8 for three out of four WRPs in the OIFS-HRA-15m configuration, hence we argue that the OIFS-
462   HRA-15m has the most realistic representation of the weather regimes pattern out of all experiments here. Large improvement
463   in OIFS-HRA-15m over the other configurations could be due to better resolved topography and land-sea contrasts.

464

465   **3.4 Discussion and Conclusions**

466   We have investigated the sensitivity of the climate biases in the OpenIFS atmosphere model to changes in horizontal resolution
467   and time step by analyzing AMIP simulations for the period 1979-2019 (**Table 1**). The strong positive surface zonal wind bias
468   over the Southern Ocean and Northern Hemisphere mid-latitudes and the negative bias in the tropical and subtropical regions
469   have significantly improved in the high horizontal resolution configuration with a short time step (~25km, OIFS-HRA-15m).
470   A similar improvement is observed at the coarse horizontal resolution version with a shorter time step (~100 km with 30 or
471   15-minutes). The zonal wind bias over the mid-latitudes in both hemispheres is reduced throughout the air column when a
472   smaller time step is used in the coarse resolution version, and we find that the changes in the surface winds are largely due to
473   enhanced shallow and mid-level convection which increases vertical momentum transport. Biases in the surface westerlies in
474   midlatitudes are common in CMIP-class climate models (**Bracegirdle et al., 2020**) and a sensitivity to friction has been noted

479 in idealized model studies (**Chen and Plumb, 2009**). We hypothesize that the enhanced shallow and mid-level convection
480 with a shorter model time step and/or increased horizontal resolution deepened the layer over which friction acts in the lower
481 troposphere so that the frictional effects on the barotropic jet increased, leading to a poleward shift in the jet and reduced biases
482 in zonal wind.
483
484 We also find a notable improvement in the representation of the Rossby wave amplitude and phase speed with increased
485 horizontal resolution and shorter time step at least for the waves accounting for most variability in both austral and boreal
486 winter seasons. The reduced zonal wind throughout the troposphere with a shorter time step (**Fig. 3**) would decrease the
487 eastward phase speed of Rossby waves, which may explain part of the reduced phase speeds (**Fig. 6**) and reduced biases.
488 However, changes in air-sea interactions or eddy-mean flow interactions may also play a role. In particular, we note that a very
489 large reduction in phase speed biases in austral winter in OIFS-LRA-15m compared to OIFS-LRA-1h were concurrent with
490 very large reduction in zonal surface wind biases.
491
492 The weather regime patterns are also more realistic in the high horizontal resolution and short time step configuration OIFS-
493 HRA-15m than OIFS-LRA-1h, but we note that there is no consistent improvement from OIFS-LRA-1h to OIFS-HRA-15m
494 as either horizontal resolution is increased or time step is shortened. For example, both OIFS-MRA-15m and OIFS-LRA-15m
495 are worse than OIFS-LRA-1h. The improvements in the weather regime patterns and Rossby wave amplitude and speed could
496 very well be related to each other as e.g. variations in Rossby wave breaking have been linked to the onset of NAO phases
497 (**Strong and Magnusdottir, 2008**) but this would require further and more targeted analysis. The overall good representation
498 of weather regimes in OIFS-LRA-1h compared to simulations with shorter time steps (OIFS-LRA-30m, OIFS-LRA-15m) may
499 be due to compensation of errors. For example, it is possible that improving the wave amplitudes and phase speeds in OIFS-
500 LRA-30m compared to OIFS-LRA-1h exposes the effect of a biases caused by both the coarse resolution in both
501 configurations, e.g., weak interactions with topography, leading to an overall worse representation of weather regimes.
502 We found a gradual reduction in SAT biases in OpenIFS with increased resolution or shorter time steps. The improvements
503 were largely driven by improvements over North America and eastern Russia. **Roberts et al. (2018)** noted similar SAT biases
504 and linked them to surface albedo, which is thus likely the cause here as well. The improvement with increased resolution
505 and/or shorter time step may be a result of improved snow cover. Systematic improvements in the precipitation biases were
506 not observed. Instead, precipitation biases generally increased with finer horizontal resolution or shorter time step, suggesting
507 that some tuning may be required in the physics parameters when changing horizontal resolution and time step.
508
509 We stress that the results presented in this study are specific to the OpenIFS atmosphere model and are crucial for the modeling
510 community that uses the OpenIFS in their climate models such as EC-Earth (**Haarsma et al., 2020; Döscher et al., 2022**),
511 CNRM (**Voldoire et al., 2019**), AWI (**Streffing et al., 2022**), and GEOMAR (**Kjellsson et al., 2020**). However, the results
512 may also have implications for other climate modeling communities, at least for those that use a semi-Lagrangian scheme

514 similar to the IFS **(e.g.,Walters et al., 2019)** in the atmospheric component where long time steps are both possible and often
515 desirable to reduce the computational cost of the model.

516

517 The zonal wind bias improvement in the OpenIFS is important for research questions linked with the Southern Ocean climate
518 dynamics that plays a crucial role in both the global atmosphere and ocean circulation. We propose that the model time step
519 not be longer than 30 minutes at any horizontal resolution to minimize surface wind biases over the ocean. The computational
520 cost increases linearly with dt (time step), whereas the cost scales with horizontal resolution as dx^3 as the number of grid
521 points increases in both dimensions and the time step is likely shortened as well. Hence, reducing the model time step from 45
522 or 60 minutes to 20 or 30 minutes may double the computational cost, but lead to significant improvements in the simulated
523 climate. The optimal model time step for the OpenIFS coarse resolution model (1°) is suggested to be 30-minute, but should
524 likely be somewhat shorter, e.g., 15 min, for higher resolutions.

525

526 **Code and data availability**

527 The OpenIFS model requires a software license agreement with ECMWF, and OpenIFS' license is easily given free of charge
528 to any academic or research institute. The details of the different versions of the OpenIFS model, including the OpenIFS
529 version used in this study, i.e., 43R3, can be found at https://confluence.ecmwf.int/display/OIFS/About+OpenIFS. The
530 OpenIFS model source code has been made available for the editor and reviewers.
531 The input datasets (both initial and boundary conditions) needed to run the OpenIFS model, run scripts, the model output, and
532 the Jupiter notebook that support the finding of this study are available at **(Savita, 2023)**. The source code for XIOS 2.5,
533 revision 1910, is available from the official repository at https://forge.ipsl.jussieu.fr/ioserver/ under CeCILL_V2 license.
534 OpenIFS experiments were made using ESM-Tools (https://github.com/esm-tools/esm_tools/). The OASIS coupler is
535 available at https://oasis.cerfacs.fr/en/. The XIOS, ESM-Tools and OASIS coupler used in this study can be downloaded from
536 https://doi.org/10.5281/zenodo.8189718.
537 The observational datasets used to validate OpenIFS model results in this study are downloaded from the ERA5
538 (https://cds.climate.copernicus.eu/), GPCP (https://psl.noaa.gov/data/gridded/data.gpcp.html) and CRUTEM4
539 (http://badc.nerc.ac.uk/data/cru/) websites. Total model output exceeds 10 Tb and it not publicly available, but is available
540 from the authors upon reasonable requests.

541 **Author contributions**

542 All the model simulations were conducted by AS and JK. Analysis of the output and the writing of text for this paper
543 coordinated by Savita with substantial contributions from JK, RPK, ML, TR, SW and WP.

Competing interest

The authors declare that they have no conflict of interest.

Acknowledgement

AS, JK and MK are supported by JPI Climate/Ocean (ROADMAP project grant 01LP2002C). We wish to thank the OpenIFS team at ECMWF for the technical support. All simulations were performed on the HLRN machine under shk00018 project resources. All analyses were performed on computer clusters at GEOMAR and Kiel University Computing Center (NESH). We thanks to Anton Beljaars for discussion on ECMWF model physics.

References

Athanasiadis, P. J., Ogawa, F., Omrani, N.-E., Keenlyside, N., Schiemann, R., Baker, A. J., Vidale, P. L., Bellucci, A., Ruggieri, P., and Haarsma, R.: Mitigating climate biases in the midlatitude North Atlantic by increasing model resolution: SST gradients and their relation to blocking and the jet, Journal of Climate, 35, 3385-3406, 2022.

Bayr, T., Latif, M., Dommenget, D., Wengel, C., Harlaß, J., and Park, W.: Mean-state dependence of ENSO atmospheric feedbacks in climate models, Climate Dynamics, 50, 3171-3194, 2018.

Beljaars, A., Balsamo, G., Bechtold, P., Bozzo, A., Forbes, R., Hogan, R. J., Köhler, M., Morcrette, J.-J., Tompkins, A. M., and Viterbo, P.: The numerics of physical parametrization in the ECMWF model, Frontiers in Earth Science, 6, 137, 2018.

Bracegirdle, T., Holmes, C., Hosking, J., Marshall, G., Osman, M., Patterson, M., and Rackow, T.: Improvements in circumpolar Southern Hemisphere extratropical atmospheric circulation in CMIP6 compared to CMIP5, Earth and Space Science, 7, e2019EA001065, 2020.

Branković, C. and Gregory, D.: Impact of horizontal resolution on seasonal integrations, Climate Dynamics, 18, 123-143, 2001.

Chen, G. and Plumb, R. A.: Quantifying the eddy feedback and the persistence of the zonal index in an idealized atmospheric model, Journal of the atmospheric sciences, 66, 3707-3720, 2009.

Couldrey, M. P., Gregory, J. M., Boeira Dias, F., Dobrohotoff, P., Domingues, C. M., Garuba, O., Griffies, S. M., Haak, H., Hu, A., and Ishii, M.: What causes the spread of model projections of ocean dynamic sea-level change in response to greenhouse gas forcing?, Climate Dynamics, 56, 155-187, 2021.

Dawson, A., Palmer, T., and Corti, S.: Simulating regime structures in weather and climate prediction models, Geophysical Research Letters, 39, 2012.

Döscher, R., Acosta, M., Alessandri, A., Anthoni, P., Arsouze, T., Bergman, T., Bernardello, R., Boussetta, S., Caron, L. P., Carver, G., Castrillo, M., Catalano, F., Cvijanovic, I., Davini, P., Dekker, E., Doblas-Reyes, F. J., Docquier, D., Echevarria, P., Fladrich, U., Fuentes-Franco, R., Gröger, M., v. Hardenberg, J., Hieronymus, J., Karami, M. P., Keskinen, J. P., Koenigk, T., Makkonen, R., Massonnet, F., Ménégoz, M., Miller, P. A., Moreno-Chamarro, E., Nieradzik, L., van Noije, T., Nolan, P., O'Donnell, D., Ollinaho, P., van den Oord, G., Ortega, P., Prims, O. T., Ramos, A., Reerink, T., Rousset, C., Ruprich-Robert, Y., Le Sager, P., Schmith, T., Schrödner, R., Serva, F., Sicardi, V., Sloth Madsen, M., Smith, B., Tian, T., Tourigny, E., Uotila, P., Vancoppenolle, M., Wang, S., Wårlind, D., Willén, U., Wyser, K., Yang, S., Yepes-Arbós, X., and Zhang, Q.: The EC-

Formatted: English (US)

580   Earth3 Earth system model for the Coupled Model Intercomparison Project 6, Geosci. Model Dev., 15, 2973-3020,
581   10.5194/gmd-15-2973-2022, 2022.

582   Eyring, V., Bony, S., Meehl, G. A., Senior, C. A., Stevens, B., Stouffer, R. J., and Taylor, K. E.: Overview of the Coupled
583   Model Intercomparison Project Phase 6 (CMIP6) experimental design and organization, Geoscientific Model Development,
584   9, 1937-1958, 2016.

585   Fabiano, F., Meccia, V. L., Davini, P., Ghinassi, P., and Corti, S.: A regime view of future atmospheric circulation changes in
586   northern mid-latitudes, Weather and Climate Dynamics, 2, 163-180, 2021.

587   Fabiano, F., Christensen, H., Strommen, K., Athanasiadis, P., Baker, A., Schiemann, R., and Corti, S.: Euro-Atlantic weather
588   Regimes in the PRIMAVERA coupled climate simulations: impact of resolution and mean state biases on model performance,
589   Climate Dynamics, 54, 5031-5048, 2020.

590   Flato, G., Marotzke, J., Abiodun, B., Braconnot, P., Chou, S. C., Collins, W., Cox, P., Driouech, F., Emori, S., and Eyring, V.:
591   Evaluation of climate models, in: Climate change 2013: the physical science basis. Contribution of Working Group I to the
592   Fifth Assessment Report of the Intergovernmental Panel on Climate Change, Cambridge University Press, 741-866, 2014.

593   Forbes, R. and Tompkins, A.: An improved representation of cloud and precipitation, ECMWF Newsletter, 129, 13-18, 2011.

594   Gates, W. L., Boyle, J. S., Covey, C., Dease, C. G., Doutriaux, C. M., Drach, R. S., Fiorino, M., Gleckler, P. J., Hnilo, J. J.,
595   and Marlais, S. M.: An overview of the results of the Atmospheric Model Intercomparison Project (AMIP I), Bulletin of the
596   American Meteorological Society, 80, 29-56, 1999.

597   Gelaro, R., McCarty, W., Suárez, M. J., Todling, R., Molod, A., Takacs, L., Randles, C. A., Darmenov, A., Bosilovich, M. G.,
598   and Reichle, R.: The modern-era retrospective analysis for research and applications, version 2 (MERRA-2), Journal of
599   climate, 30, 5419-5454, 2017.

600   Haarsma, R., Acosta, M., Bakhshi, R., Bretonnière, P.-A. B., Caron, L.-P., Castrillo, M., Corti, S., Davini, P., Exarchou, E.,
601   and Fabiano, F.: HighResMIP versions of EC-Earth: EC-Earth3P and EC-Earth3P-HR. Description, model performance, data
602   handling and validation, (No Title), 2020.

603   Harris, I., Jones, P. D., Osborn, T. J., and Lister, D. H.: Updated high-resolution grids of monthly climatic observations–the
604   CRU TS3. 10 Dataset, International journal of climatology, 34, 623-642, 2014.

Hazeleger, W., Wang, X., and Severijns, C.: SS tef anescu, R Bintanja, A Sterl, Klaus Wyser, T Semmler, S Yang, B Van den Hurk, et al. Ec-earth v2. 2: description and validation of a new seamless earth system prediction model, Climate dynamics, 39, 2611-2629, 2012.

He, C. and Zhou, T.: The two interannual variability modes of the western North Pacific subtropical high simulated by 28 CMIP5–AMIP models, Climate dynamics, 43, 2455-2469, 2014.

Hersbach, H., Bell, B., Berrisford, P., Hirahara, S., Horányi, A., Muñoz-Sabater, J., Nicolas, J., Peubey, C., Radu, R., and Schepers, D.: The ERA5 global reanalysis, Quarterly Journal of the Royal Meteorological Society, 146, 1999-2049, 2020.

Hogan, R. J. and Bozzo, A.: A flexible and efficient radiation scheme for the ECMWF model, Journal of Advances in Modeling Earth Systems, 10, 1990-2008, 2018.

Huffman, G. J., Adler, R. F., Arkin, P., Chang, A., Ferraro, R., Gruber, A., Janowiak, J., McNab, A., Rudolf, B., and Schneider, U.: The global precipitation climatology project (GPCP) combined precipitation dataset, Bulletin of the american meteorological society, 78, 5-20, 1997.

Jung, T., Miller, M., Palmer, T., Towers, P., Wedi, N., Achuthavarier, D., Adams, J., Altshuler, E., Cash, B., and Kinter Iii, J.: High-resolution global climate simulations with the ECMWF model in Project Athena: Experimental design, model climate, and seasonal forecast skill, Journal of Climate, 25, 3155-3172, 2012.

Kim, S. T., Cai, W., Jin, F.-F., and Yu, J.-Y.: ENSO stability in coupled climate models and its association with mean state, Climate dynamics, 42, 3313-3321, 2014.

Kjellsson, J., Streffing, J., Carver, G., and Köhler, M.: From weather forecasting to climate modelling using OpenIFS, ECMWF Newsletter, 164, 38-41, 2020.

Liu, B., Gan, B., Cai, W., Wu, L., Geng, T., Wang, H., Wang, S., Jing, Z., and Jia, F.: Will increasing climate model resolution be beneficial for ENSO simulation?, Geophysical Research Letters, 49, e2021GL096932, 2022.

Ma, P.-L., Harrop, B. E., Larson, V. E., Neale, R. B., Gettelman, A., Morrison, H., Wang, H., Zhang, K., Klein, S. A., and Zelinka, M. D.: Better calibration of cloud parameterizations and subgrid effects increases the fidelity of the E3SM Atmosphere Model version 1, Geoscientific Model Development, 15, 2881-2916, 2022.

Matthes, K., Biastoch, A., Wahl, S., Harlaß, J., Martin, T., Brücher, T., Drews, A., Ehlert, D., Getzlaff, K., and Krüger, F.: The flexible ocean and climate infrastructure version 1 (FOCI1): Mean state and variability, Geoscientific Model Development, 13, 2533-2568, 2020.

Meehl, G. A. and Teng, H.: CMIP5 multi-model hindcasts for the mid-1970s shift and early 2000s hiatus and predictions for 2016–2035, Geophysical Research Letters, 41, 1711-1716, 2014.

Meng, Y., Hao, Z., Feng, S., Guo, Q., and Zhang, Y.: Multivariate bias corrections of CMIP6 model simulations of compound dry and hot events across China, Environmental Research Letters, 17, 104005, 2022.

Osborn, T. and Jones, P.: The CRUTEM4 land-surface air temperature data set: construction, previous versions and dissemination via Google Earth, Earth System Science Data, 6, 61-68, 2014.

Pilch Kedzierski, R., Matthes, K., and Bumke, K.: New insights into Rossby wave packet properties in the extratropical UTLS using GNSS radio occultations, Atmospheric Chemistry and Physics, 20, 11569-11592, 2020.

Roberts, C. D., Senan, R., Molteni, F., Boussetta, S., Mayer, M., and Keeley, S. P.: Climate model configurations of the ECMWF Integrated Forecasting System (ECMWF-IFS cycle 43r1) for HighResMIP, Geoscientific model development, 11, 3681-3712, 2018.

Savita, A.: Assessment of Climate Biases in OpenIFS Version 43R3 across Model Horizontal Resolutions and Time Steps [dataset], https://hdl.handle.net/20.500.12085/c74887dc-e609-4392-9faf-48c67276d5d1, 2023.

Simmons, A. J. and Burridge, D. M.: An energy and angular-momentum conserving vertical finite-difference scheme and hybrid vertical coordinates, Monthly Weather Review, 109, 758-766, 1981.

Streffing, J., Sidorenko, D., Semmler, T., Zampieri, L., Scholz, P., Andrés-Martínez, M., Koldunov, N., Rackow, T., Kjellsson, J., and Goessling, H.: AWI-CM3 coupled climate model: description and evaluation experiments for a prototype post-CMIP6 model, Geoscientific Model Development, 15, 6399-6427, 2022.

Strong, C. and Magnusdottir, G.: Tropospheric Rossby wave breaking and the NAO/NAM, Journal of the atmospheric sciences, 65, 2861-2876, 2008.

Taylor, K. E., Stouffer, R. J., and Meehl, G. A.: An overview of CMIP5 and the experiment design, Bulletin of the American meteorological Society, 93, 485-498, 2012.

Temperton, C., Hortal, M., and Simmons, A.: A two-time-level semi-Lagrangian global spectral model, Quarterly Journal of the Royal Meteorological Society, 127, 111-127, 2001.

Tiedtke, M.: Representation of clouds in large-scale models, Monthly Weather Review, 121, 3040-3061, 1993.

657 Voldoire, A., Saint-Martin, D., Sénési, S., Decharme, B., Alias, A., Chevallier, M., Colin, J., Guérémy, J. F., Michou, M., and
658 Moine, M. P.: Evaluation of CMIP6 deck experiments with CNRM-CM6-1, Journal of Advances in Modeling Earth Systems,
659 11, 2177-2213, 2019.

660 Walters, D., Baran, A. J., Boutle, I., Brooks, M., Earnshaw, P., Edwards, J., Furtado, K., Hill, P., Lock, A., and Manners, J.:
661 The Met Office Unified Model global atmosphere 7.0/7.1 and JULES global land 7.0 configurations, Geoscientific Model
662 Development, 12, 1909-1963, 2019.

663 Williamson, D. L., Kiehl, J. T., and Hack, J. J.: Climate sensitivity of the NCAR Community Climate Model (CCM2) to
664 horizontal resolution, Climate Dynamics, 11, 377-397, 1995.

665 Wolf, G. and Wirth, V.: Diagnosing the horizontal propagation of Rossby wave packets along the midlatitude waveguide,
666 Monthly Weather Review, 145, 3247-3264, 2017.

667 Zhou, S., Huang, G., and Huang, P.: Excessive ITCZ but negative SST biases in the tropical Pacific simulated by CMIP5/6
668 models: The role of the meridional pattern of SST bias, Journal of Climate, 33, 5305-5316, 2020.

669 **Table**

670

Experiment Name	Horizontal resolution	Vertical grid	Time step	CHPSY	SYPD
OIFS-LRA-15m	Tco95/100km	L91	15m	3.3 k	11
OIFS-MRA-15m	Tco199/50km	L91	15m	13.3 k	4
OIFS-HRA-15m	Tco399/25km	L91	15m	19.2 k	2
OIFS-LRA-30m	Tco95/100km	L91	30m	845	21
OIFS-LRA-1h	Tco95/100km	L91	1h	256	36

671

672 **Table 1**. List of the experiments performed across different horizontal resolutions and model time steps using OIFS model.
673 In the above table CHPSY is core hours per simulation year, and SYPD is simulation year per day.
674
675

676 **Figures**

677
678
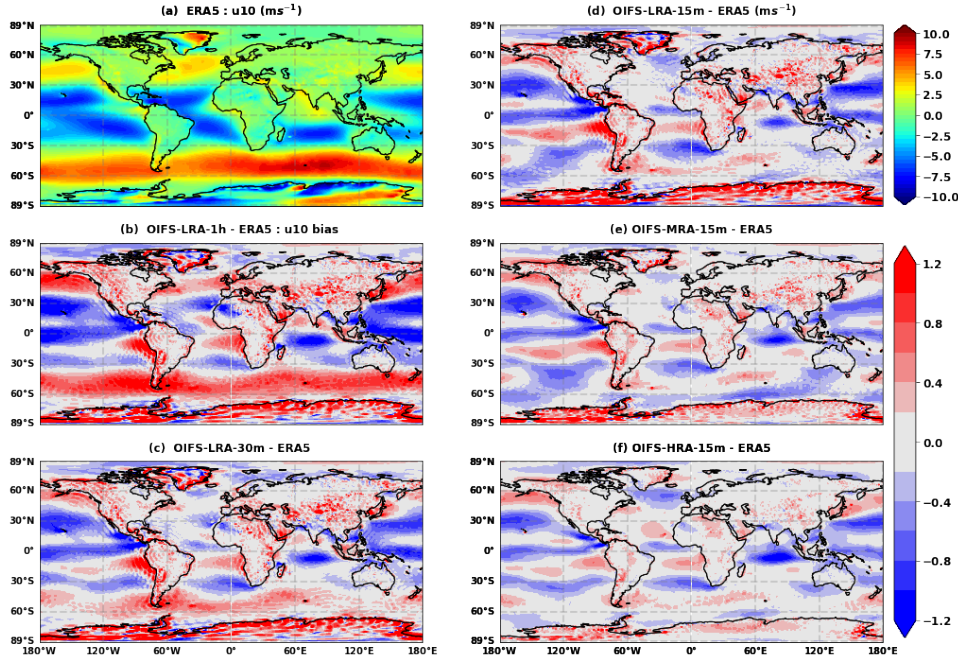
Figure 1. (a) Annual mean ERA5 surface zonal wind [ms⁻¹]. (b-d) Annual mean zonal wind [ms⁻¹] bias for different model time steps (1h (b), 30m (c), and 15m (d)) using ~100 km resolution, and (e-f) with different horizontal resolutions, ~50 (e) and ~25 km (f), respectively. Biases are computed with respect to ERA5 over the period 1979–2019.

682
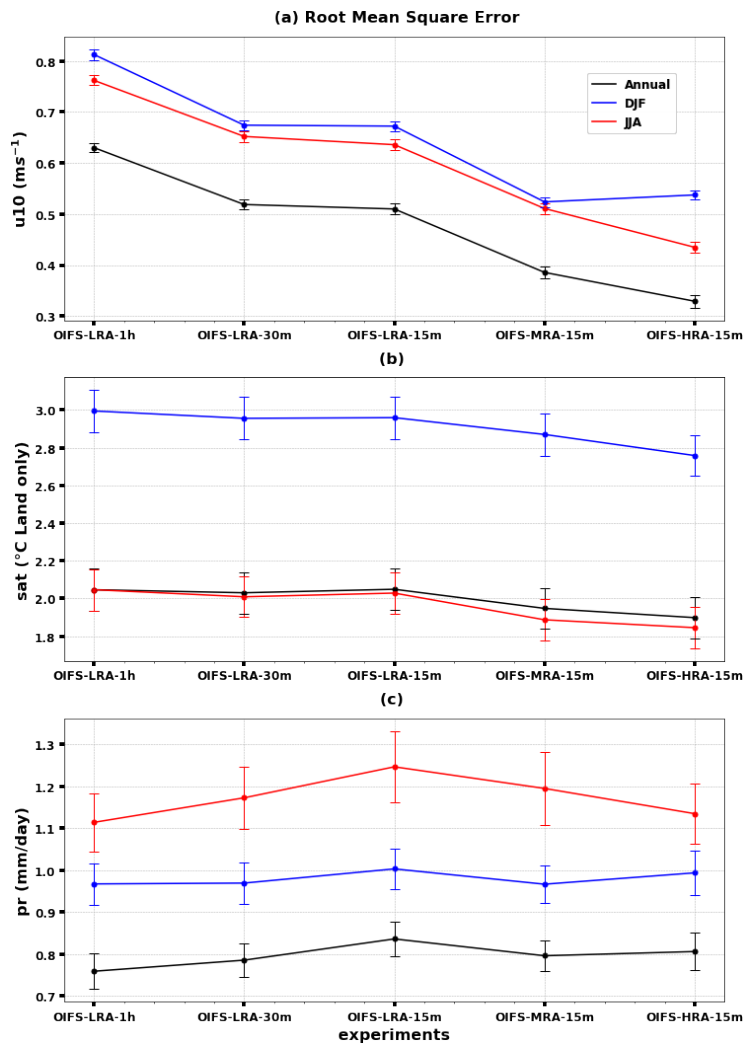
683

684 **Figure 2**. Root mean squared error of surface zonal wind (a), SAT (b), and precipitation (c) over the period 1979-2019 for all

685 the configurations: annual (black) and seasonal mean (DJF: blue, JJA: red). The error bars represent a 95% confidence interval.
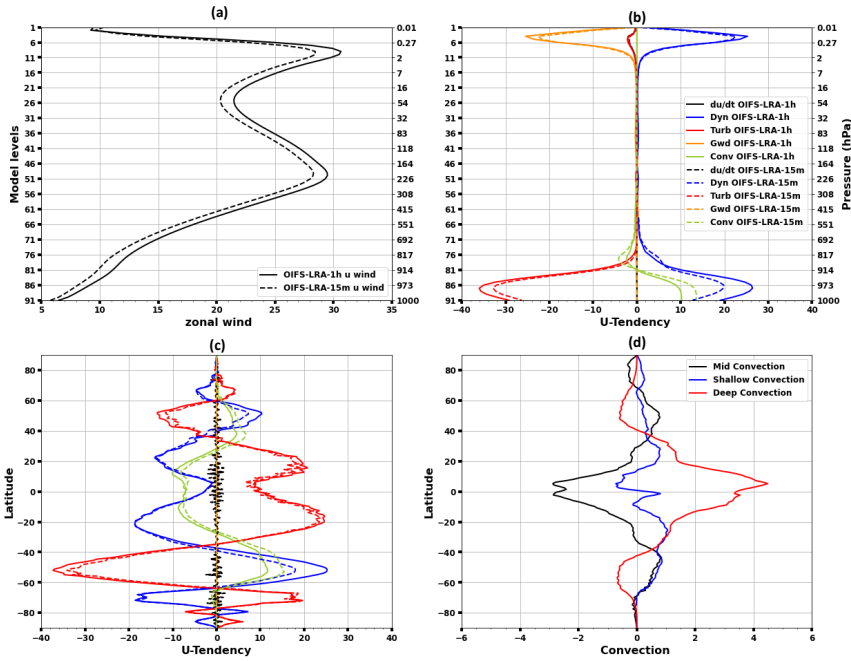
Figure 3. (a) Averaged zonal wind (u) [ms^{-1}] and zonal wind tendencies [ms^{-2}/hour] over the Southern Ocean (40°S – 60°S, all longitude) as a function of height for OIFS-LRA-1h and OIFS-LRA-15m. Model levels (y-axis left) and pressure levels (y-axis right). (c) Zonal and time average of zonal wind tendencies at the lowest level of the model as a function of latitude. (d) Zonal and time average convection difference [Kgm^{-2}/hour] between OIFS-LRA -15m and OIFS-LRA-1h configurations. The solid lines in panels (b) and (c) show the wind tendency for OIFS-LRA-1h configuration whereas the dashed lines are for OIFS-LRA-15m configuration. Shown are averages over 1979-2019.

698
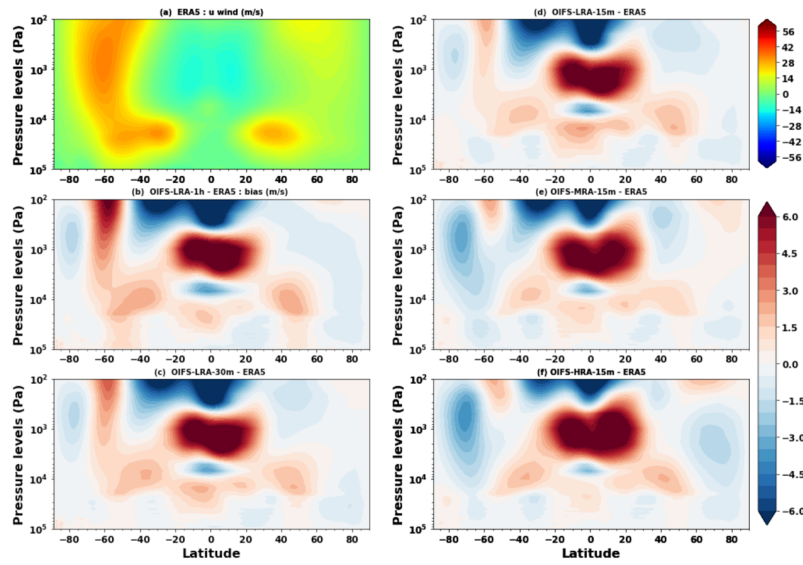
Figure 4. (a) Annual zonal mean ERA5 zonal wind [ms⁻¹]. (b-d) Annual zonal mean zonal wind [ms⁻¹] bias for different model time steps (1h (b), 30m (c), and 15m (d)) using ~100 km resolution, and (e-f) with different horizontal resolutions, ~50 (e) and ~25 km (f), respectively. Biases are computed with respect to ERA5 over the period 1979–2019.

699
700
701
702

703
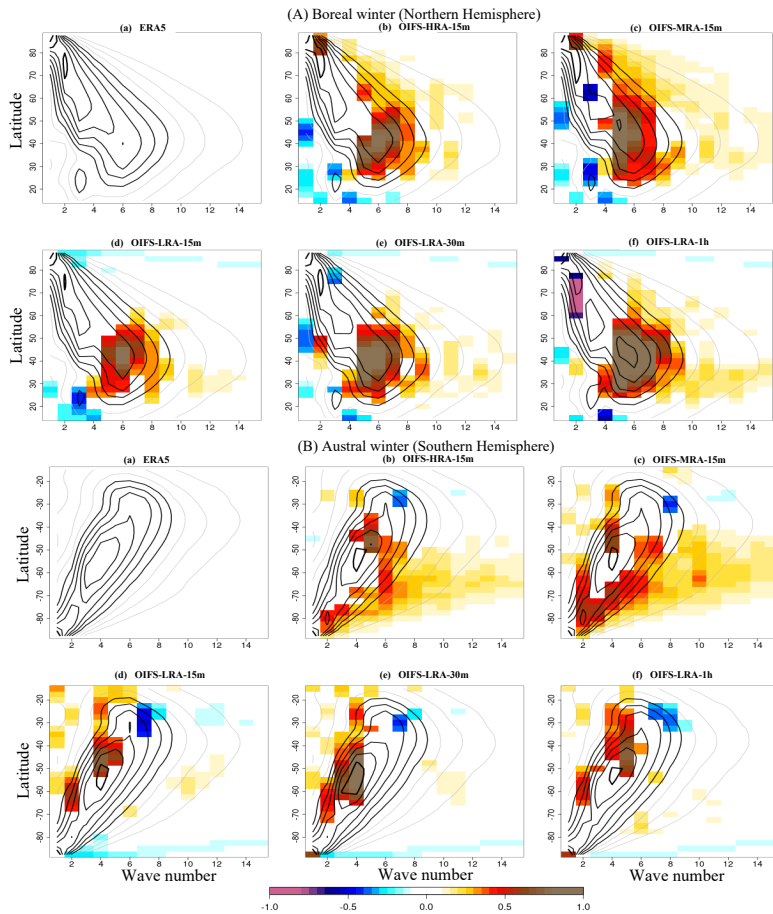
Figure 5. (A) The Rossby wave amplitude (contours) for different wave numbers in the Northern Hemisphere at 300 hPa (a)
in ERA5 observation and (b-f) in the OIFS model simulations during 1979-2019 in DJF (i.e., boreal winter). The color shows
difference of wave amplitude between the model and ERA5 where it is significant on the 95 % confidence level. The wave
amplitude and contour interval are shown in ms^{-1}. The grey contours start from 2 ms^{-1} and the black contours from 5 ms^{-1} and
the contour interval is 1 ms^{-1}. (B) is similar to (A), but for JJA (i.e., austral winter).

711
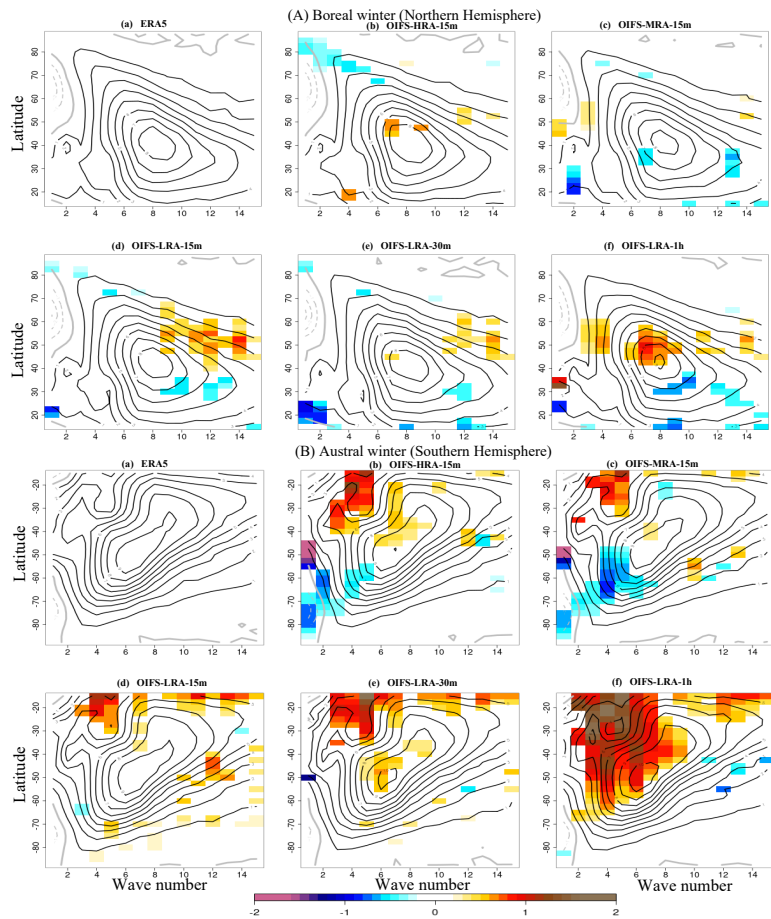
Figure 6. (A) The Rossby wave phase speed (contours) for different wave numbers at 300 hPa in the Northern Hemisphere in
ERA5 (a) observation and (b-f) in the OIFS model simulations during 1979-2019 in DJF (i.e., boreal winter). The color shows
the difference of wave phase speed between model and ERA5 where it is significant on the 95 % confidence level. The wave
phase speed and contour interval are shown in ms^{-1}. The black contours start from 1 ms^{-1}and the contour interval is 1 ms^{-1}.
Panel (B) is similar to panel (A), but for JJA (i.e., austral winter). The dahs contours show a negative phase speed and a gray
contour shows a zero-phase speed.
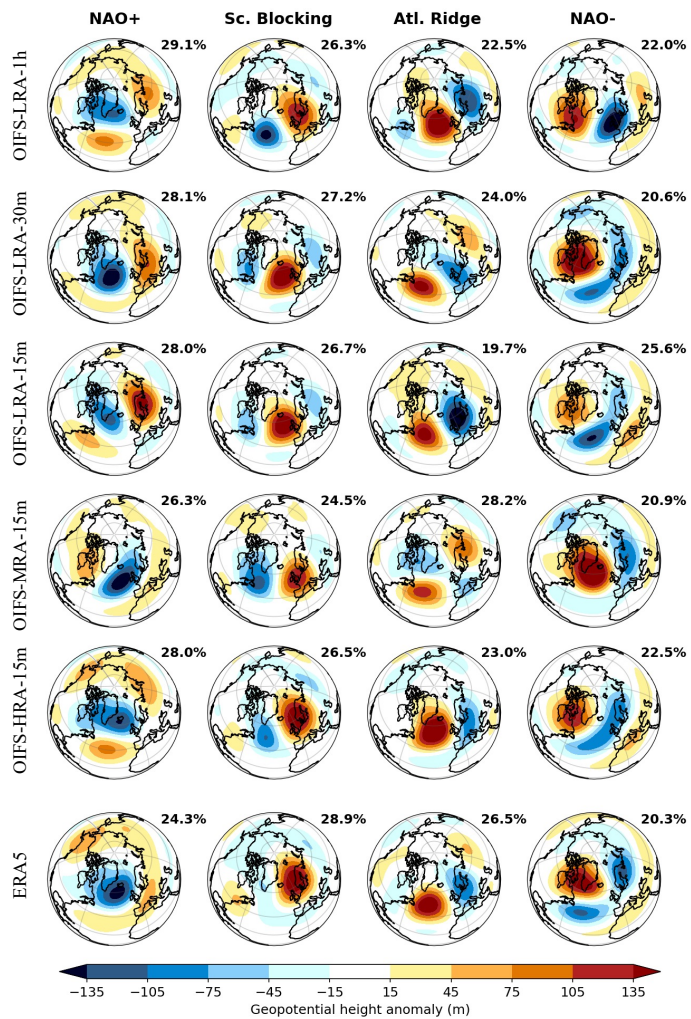
720
721
Figure. 7. Weather regime patterns over the Euro–Atlantic regions from ERA5 observation (bottom row) and the individual OIFS model simulations (1st to 5th row) over the time period 1979–2019 for DJF (boreal winter season).

725

726
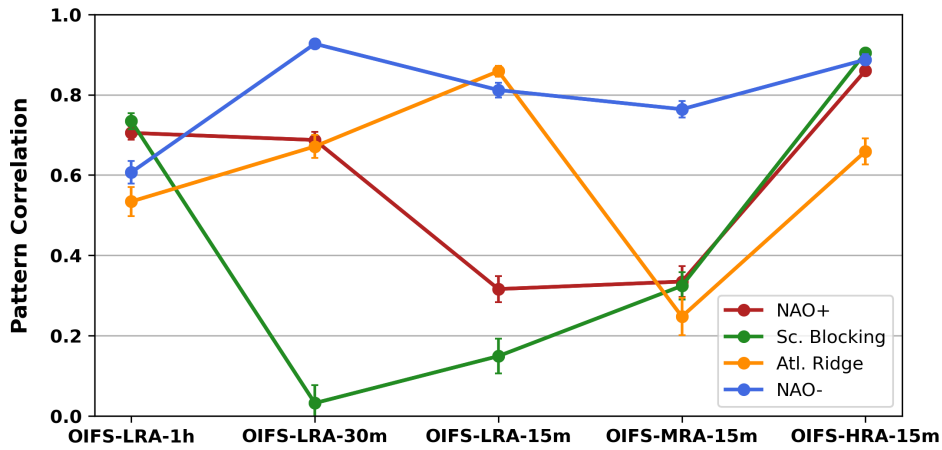
Figure. &, Pattern correlation coefficient of the individual weather regime between OIFS model configurations and ERA5 for

the period 1979-2019 for the DJF season. The error bars represent a 95% confidence interval.

729

730

731

732

Deleted: 7